remote sensing

MDPI

Article

On the Use of Tri-Stereo Pleiades Images for the Morphometric Measurement of Dolines in the Basaltic Plateau of Azrou (Middle Atlas, Morocco)

Maria Teresa Melis [1], Luca Pisani [2,*] and Jo De Waele [2]

[1] Department of Chemical and Geological Sciences, University of Cagliari, Cittadella Universitaria-S.S. 554 Bivio per Sestu I, 09042 Monserrato, Cagliari, Italy; titimelis@unica.it
[2] Department of Biological, Geological and Environmental Sciences, University of Bologna, Via Zamboni 67, 40126 Bologna, Italy; jo.dewaele@unibo.it
* Correspondence: luca.pisani4@unibo.it

Abstract: Hundreds of large and deep collapse dolines dot the surface of the Quaternary basaltic plateau of Azrou, in the Middle Atlas of Morocco. In the absence of detailed topographic maps, the morphometric study of such a large number of features requires the use of remote sensing techniques. We present the processing, extraction, and validation of depth measurements of 89 dolines using tri-stereo Pleiades images acquired in 2018–2019 (the European Space Agency (ESA) © CNES 2018, distributed by Airbus DS). Satellite image-derived DEMs were field-verified using traditional mapping techniques, which showed a very good agreement between field and remote sensing measures. The high resolution of these tri-stereo images allowed to automatically generate accurate morphometric datasets not only regarding the planimetric parameters of the dolines (diameters, contours, orientation of long axes), but also for what concerns their depth and altimetric profiles. Our study demonstrates the potential of using these types of images on rugged morphologies and for the measurement of steep depressions, where traditional remote sensing techniques may be hindered by shadow zones and blind portions. Tri-stereo images might also be suitable for the measurement of deep and steep depressions (skylights and collapses) on Martian and Lunar lava flows, suitable targets for future planetary cave exploration.

Keywords: remote sensing; karst; sinkholes; morphometry; collapse; GIS

Citation: Melis, M.T.; Pisani, L.; De Waele, J. On the Use of Tri-Stereo Pleiades Images for the Morphometric Measurement of Dolines in the Basaltic Plateau of Azrou (Middle Atlas, Morocco). *Remote Sens.* **2021**, *13*, 4087. https://doi.org/10.3390/rs13204087

Academic Editors: Francesca Giannone and Valerio Baiocchi

Received: 31 August 2021
Accepted: 8 October 2021
Published: 13 October 2021

1. Introduction

Geological landscapes and structures can be easily studied starting from high spatial resolution Digital Elevation Models (DEMs) and a set of useful tools able to extract specific landforms and quantify geomorphological parameters [1–3]. Moreover, topographical maps of sufficient scale and precision are often not available for many regions in the world. In these areas, the combination of remote sensing data from different sources into Geographic Information Systems (GIS) allows to obtain new information and integrate them with field-based data.

The detection of karst morphologies from DEMs processing is a well-known methodology, largely applied for geomorphological studies, risk and geohazard assessment, and land use management [4–10]. Studies based on the comparison between DEM and field-based data have demonstrated that the use of digital images with an appropriate spatial resolution generally provides reliable results in the morphometric characterization of sinkholes [11,12].

The elevation model extracted from optical satellite images, however, must guarantee a quality standard. Accurate elevation and morphological details are critical points for geomorphological mapping purposes if satellite data are to be used [2]. Terrain roughness, ground resolution, base-to-height ratio, and image contrast affect the accuracy of the

produced DEMs from optical space images [12,13]. In the last years, several very-high resolution satellites were launched (e.g., QuickBird, OrbView, GeoEye-1, and the series of WorldView platforms, as well as Pleiades), with the capacity of providing images with a ground resolution of up to 0.3 m.

Conventional techniques for DEM creation, based on terrestrial surveying and aerial images and improved using GPS, have been integrated by the production of elevation models created with satellite stereoscopic images [14–16]. Optical and Synthetic Aperture Radar (SAR) are consolidated methods to obtain DEMs with different resolution and accuracy at the local, regional, and global scales. Among them, the stereoscopic triplet can be considered an improvement of the simple stereo-couple, allowing for a better retrieval of altitudes over impervious terrains, steep slopes, and shadows [17].

The Pleiades mission was the first satellite system that introduced the stereoscopic triplet, adopting a new acquisition mode, based on the nearly simultaneous acquisition of three images, one backward looking (B), one forward looking (F), plus a third near-nadir image (N) [18]. The Pleiades constellation consists of two satellites: 1A spacecraft was launched on 16 December 2011, and Pleiades 1B in late 2012. Panchromatic and multispectral data are acquired simultaneously at a nominal resolution of 0.5 m and 2 m. The products are mainly used to produce 50-cm ortho-imagery, and the acquisition of synchronous images of the same area with different looking angle, allows for obtaining very high-resolution DEMs. In particular, the use of a near-nadir (N) image improves the signal of the classical forward (F) and backward (B) looking stereo pairs, allowing a better retrieval of heights over terrains with high roughness and steep slopes characterized by large areas with shadows (Figure 1). DEMs extracted from these data proved to be well-suited for the analyses of elevation in different geomorphological environments such as mountain glaciers, volcanic ranges, and in urban areas [13,19,20]. Moreover, the use of these data is focused on the multitemporal analysis of DTMs based on multiple acquisitions with the possibility to extract surface and volume changes [13,17].

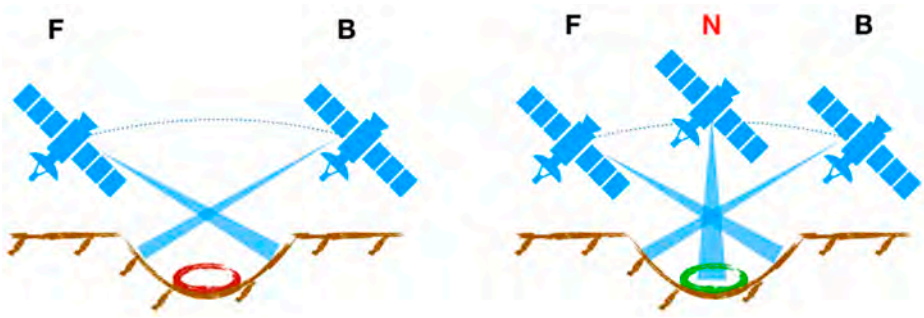

Figure 1. Stereoscopic cover capabilities over the studied surfaces with deep morphological depressions: on the left, the red region represents the area that cannot be covered by the standard stereo images; on the right, the nadir image allows to complete the visualization of the steep walls and the floor of the depression (in green).

The aim of this study is to verify the use of DEMs extracted from Pleiades tri-stereo optical data for the evaluation of morphometric parameters in the Middle Atlas in Morocco, where high resolution topographic maps are not available. In particular, this study addresses the problem of evaluating the depth of sinkhole-like depressions dotting the basaltic plateau of Azrou. Several of these "dolines" are deep and have sub-vertical walls, or are vegetated by tall Atlas cedars, and are therefore affected by shadow problems.

In this study, Pleiades tri-stereo images were used for the first time to generate DEMs and to extract morphometric parameters of these steep and deep depressions with different degrees of disturbances (shadow zones, tall trees, human-built structures, etc.). A DEM with a resolution of 5 m/pixel has been extracted from Pleiades tri-stereo imagery to obtain morphometric parameters of the doline fields in the Azrou Plateau (Table 1).

Table 1. List of the morphometric parameters generally used to characterize sinkholes, which can be automatically extracted from DEMs processing.

Morphometric Parameters	Processing
Minimum elevation (**Z_Min**)	Measured on the topographic surface surrounded by the shape
Maximum elevation (**Z_Max**)	"
Minimum slope	Measured on the sinkhole slope raster
Maximum slope	"
Depth (m)	Difference between maximum and minimum elevation
Maximum axis (m)	Measured using the bounding box of the shape
Minimum axis (m)	"
Azimuth of the maximum axis (deg)	Angular value in degrees from geographic North
Perimeter (m)	Linear measure of the shape
2D Surface (m^2)	Area of the shape
3D Surface (m^2)	Area of the topographic surface of the sinkhole
Volume (m^3)	Measured from the topographic surface and the shape of each sinkhole

Whereas planimetric measurements can be obtained at very-high resolution, less is known about the accuracy of vertical measurements, and especially the depth of such steep and rough depressions. The depth measures of the sinkholes calculated from the Pleiades-derived DEM have been compared with the same parameter collected in the field for a set of these landforms (n = 89). The morphometric measurements extracted in the GIS environment were thus used to verify the vertical accuracy of the remote-sensing derived data, and especially to assess if vertical measurements (i.e., depth of dolines) are reliable. Therefore, this study proposes a possible remote sensing workflow for the use of Pleiades-derived DEMs and the morphometric study of steep and rugged shadow-prone terrains.

2. Materials and Methods

2.1. Study Area

The Quaternary Azrou volcanic plain in the Middle Atlas of Morocco covers more than 400 km^2 [21], and well-preserved cones and calderas are still clearly visible (Figure 2) [22]. Martin surveyed over 100 large collapses in the 70–80s on the basalt plain using 1:100,000 maps and some aerial photographs [23]. Since the basalts cover the Jurassic limestones, it is not well known if these voids are karstic in origin, or if they are parts of lava tube systems. Williams defined them as "caprock collapse sinkholes" in his chapter on dolines in the Encyclopedia of Caves and Karst [24], thus suggesting the presence of karstic voids underneath. However, some small lava tube segments are known in this area [23], and some of the collapses are clearly aligned, or located at the center of the lava flows. This plateau thus offers the unique opportunity of studying collapses formed by the supposed presence of lava tubes and of karst voids (ancient doline fields or collapsed caves). Recent studies have shown a good agreement between remote-sensing derived lineaments and karst features [25,26]. These studies used LANDSAT 7 ETM+ (spatial resolution of 30 m, 15 m in panchromatic), Sentinel-2 (spatial resolution greater than 10 m), and ASTER GDEM data (spatial resolution of 30 m). The possible presence of well-developed karst systems, covered by basalts but reactivated after the emplacement of these volcanic rocks, should be taken into account when considering the vulnerability of this significant regional aquifer, with important karst springs used for drinking water purposes (e.g., Oum Er-Rbia) [26,27]. However, currently, none of the above-mentioned studies in the area used high resolution images (e.g., Pleiades).

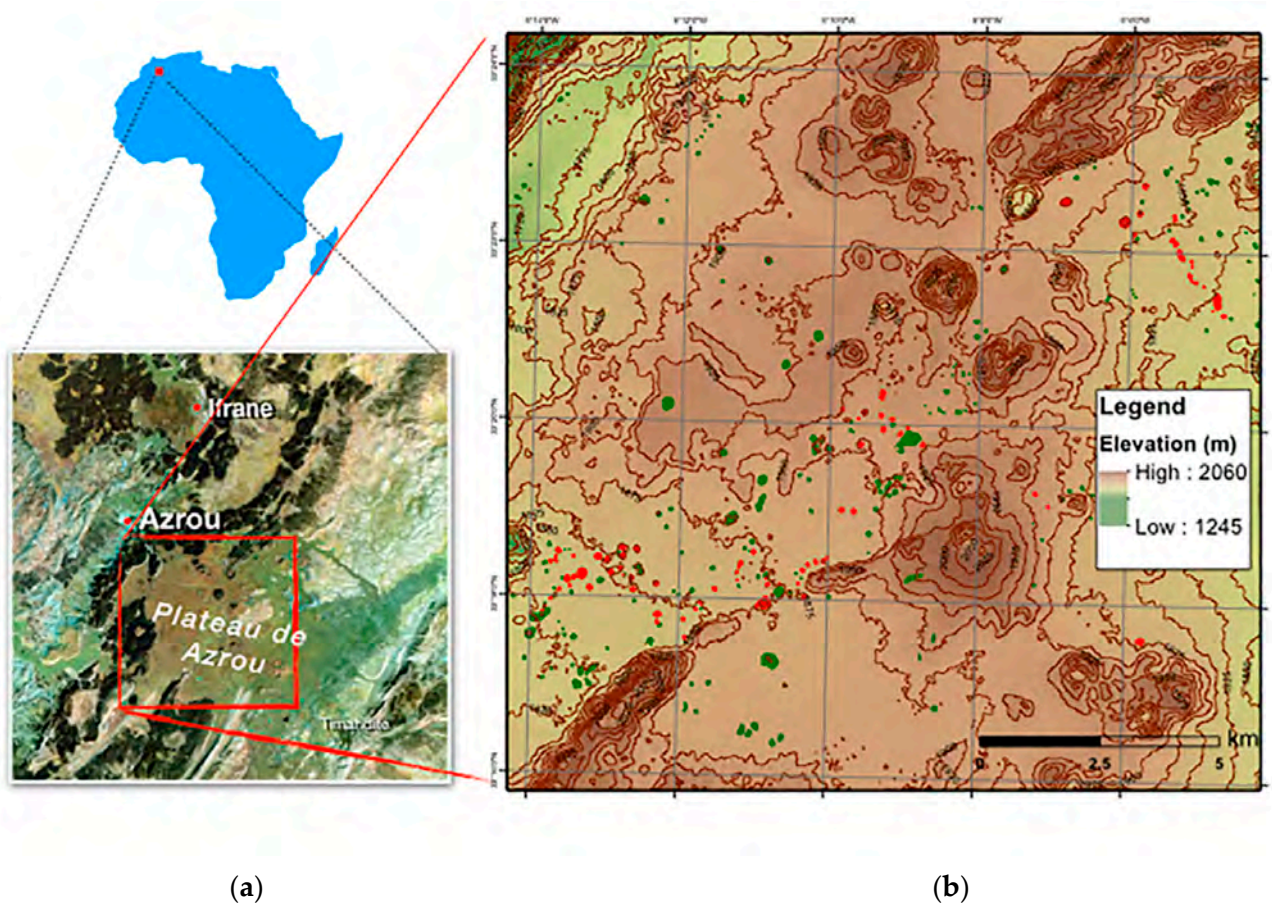

(**a**) (**b**)

Figure 2. (**a**) Localization of the study area in Central Morocco. On the DEM on the right image (**b**), volcanic cones and calderas are clearly recognizable. The sinkholes analyzed in this research are shown in red, whereas the other sinkholes are shown in green.

2.2. Satellite Imagery

During the first steps of this study, the photointerpretation of low-resolution satellite data (LANDSAT 7 ETM+, ASTER, and ESA Sentinel 2) allowed us to map 357 possible sinkholes in the Azrou plateau (Figure 3). The low resolution of these satellite images, however, did not allow us to extract detailed morphometric information on these collapses. In this study, we tested the Pleiades tri-stereo product (ground resolution of panchromatic data 0.5 m), provided by Airbus Defence and Space, to produce a very high-resolution DEM for a detailed morphological analysis.

As Pleiades tri-stereo data of the area of interest were not available, we planned an acquisition on-demand of a dedicated tri-stereo product. In order to use the high-resolution imagery for the photointerpretation of geomorphological features, ortho-images completed the list of data used in this study (Table 2). Data were acquired in 2018 and 2019 in the framework of an ESA-funded project (European Space Agency © CNES 2018, distributed by Airbus DS).

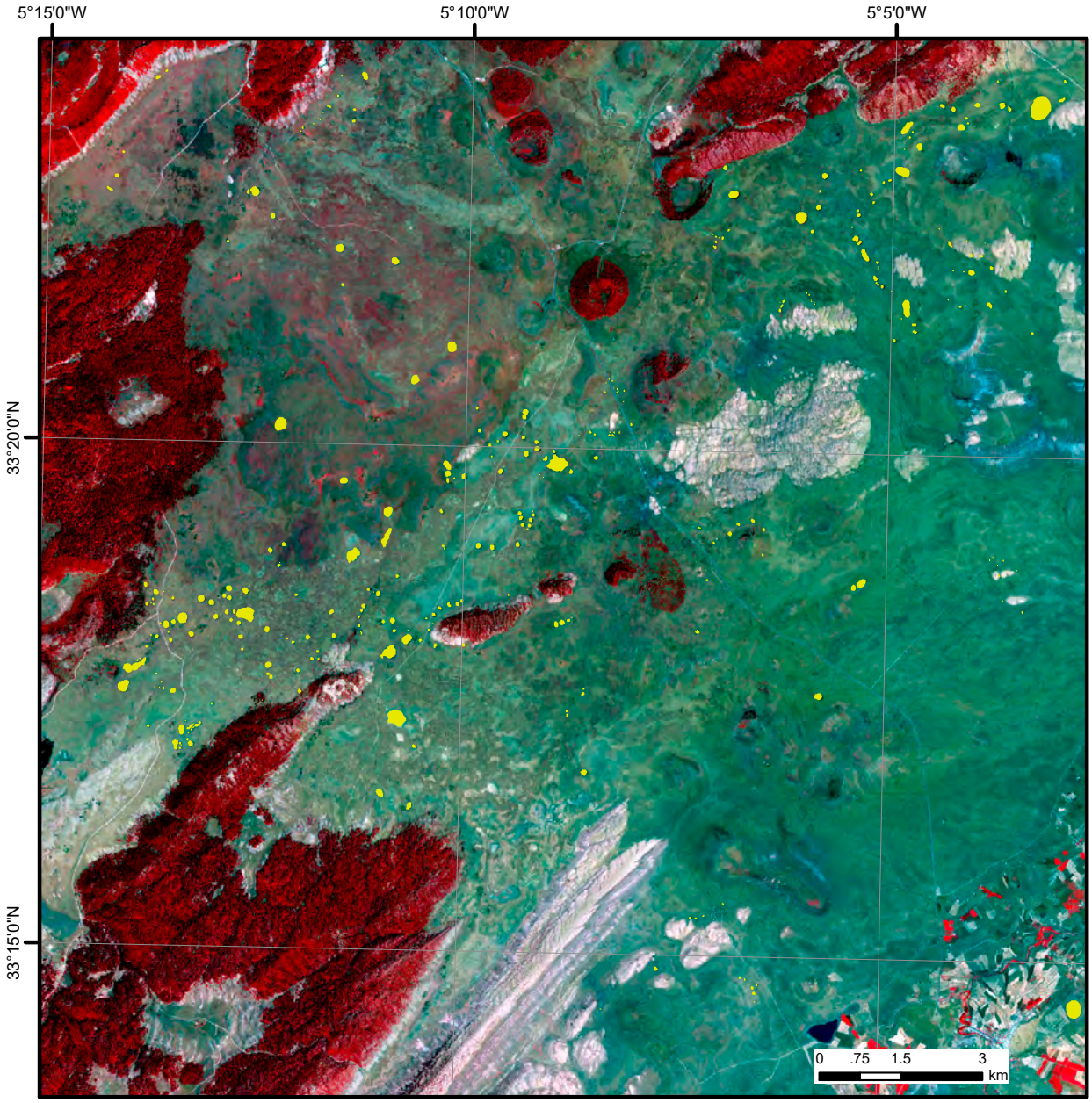

Figure 3. Sentinel 2 imagery acquired on 23 July 2016 of the Plateau of Azrou: in yellow the 357 identified sinkholes through photointerpretation.

Table 2. List of the Pleiades data acquired in this study.

Product ID	Processing Level
DS_PHR1A_201810251114401_FR1_PX_W006N33_1108_01721	SENSOR
DS_PHR1A_201810251114039_FR1_PX_W006N33_1109_01574	SENSOR
DS_PHR1A_201810251115071_FR1_PX_W006N33_1109_01646	SENSOR
DS_PHR1A_201908191122060_FR1_PX_W006N33_1206_02715	ORTHO
DS_PHR1B_201907131107426_FR1_PX_W006N33_1216_00866	ORTHO
DS_PHR1A_201908191122060_FR1_PX_W006N33_1108_00986	ORTHO
DS_PHR1B_201907131107426_FR1_PX_W006N33_1116_00824	ORTHO
DS_PHR1A_201906281122179_FR1_PX_W006N33_0910_02480	ORTHO
DS_PHR1A_201908191122494_FR1_PX_W006N33_0904_01190	ORTHO

Pleiades products were delivered in DIMAP V2 format. This file format provides, in addition to the Image file (JPEG 2000 or GeoTIFF), the RPCs (Rational Polynomial Coefficients), allowing to extract the DEM, and to apply the orthorectification and geometric processing. Moreover, a KMZ file for the localization in Google Earth environment, and the masks on data quality and cloud cover complete the data.

2.3. DEM Extraction

The IMAGINE Photogrammetry toolbox available in ERDAS IMAGINE 2014 (Version 14.00, © 1990–2013 Intergraph Corporation)) was used to process the Pleiades-1 tri-stereo data. As discussed in [13,17,28], in order to obtain the final DEM, point clouds were extracted from each image pair (F-N, F-B, and N-B), and from the merging of the resulting datasets. The application of a semi-global matching (SGM), and the use of the RPC files delivered together with the original scene, allow the orientation and georectification for the imagery. Tie points (TP) for the exterior orientation were automatically identified and improved by adding 12 ground control points (GCP). These points represent 6 sinkholes: for each one, the point of acquisition along the border and the point of maximum depth were identified in each Pleiades image. These points were added to the TPs to input the real field measures of the depth to the dataset. An overall root mean square error of less than 0.1 pixels shift between images at each TP was obtained.

The resulting merged point cloud was then gridded to a spatial resolution of 5×5 m/pixel size. The elevation value for each cell was calculated as the average elevation of all the points within one cell as proposed in [13].

2.4. Dolines Identification and Morphometric Measurements

In order to highlight the depressions, and thus facilitate their semi-automatic recognition in the DEM, a morphometric processing was applied. Following the methodology applied for geomorphological mapping in [29], a DEM-based morphometric map was produced (Figure 4). The map represents the combination of profile curvatures, with classes from negative to positive values, and the slope values. The resulting values vary from negatives (concave pixels) to positives (convex pixels).

The contours of the dolines were extracted automatically using GIS and checked with the photointerpretation of the Pleiades orthoimages. In general, the border of most collapse dolines is rather abrupt, with sinkholes opening in a surrounding flat terrain (e.g., ancient lava flow). The border thus corresponds to an abrupt change in angle, from near horizontal to steep or near vertical, and can easily be traced in the DEMs. In more gentle terrains, the knickpoints (changes from convex to concave profile) were extracted from the DEM, and elevation profiles were traced across the dolines. The position of the change of the convex curvature was compared with the existing x,y position on the shape of the same feature. Moreover, contours were extracted from the DEM and compared with the morphologies of the depressions in the orthoimage (Figure 5).

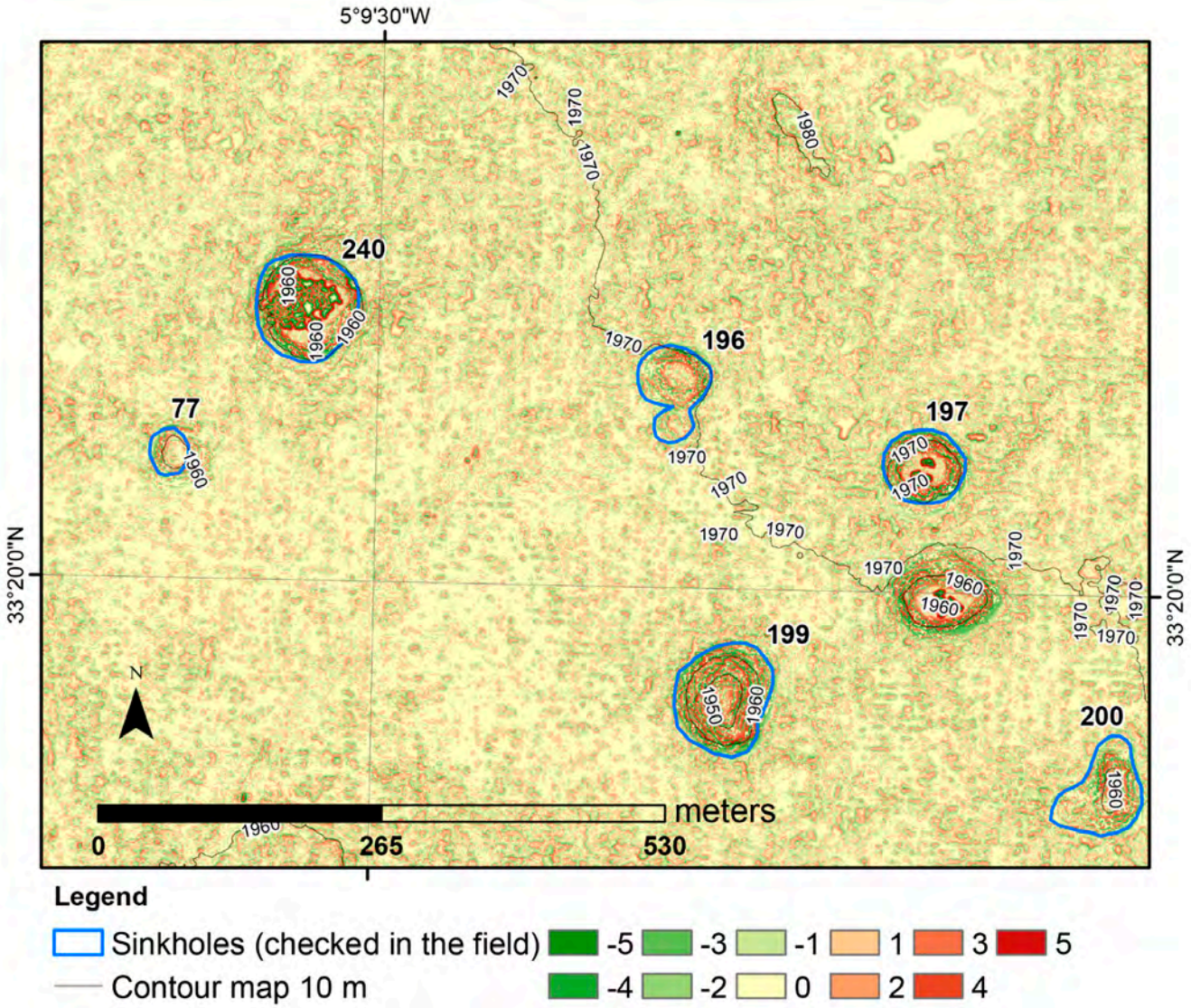

Figure 4. The morphometric map shows the overlay of the sinkholes as mapped in the field on the depressions extracted from the combination of the profile curvature and slope maps. The green color in the legend represents pixels with a negative curvature value ranging from low to high value of slope (from −5 to −1); red pixels have a positive value of curvature value, ranging from low to high value of slope (from 1 to 5). The zero value, in bright yellow, represents flat areas. Black bold numbers identify the codes given to name the mapped dolines.

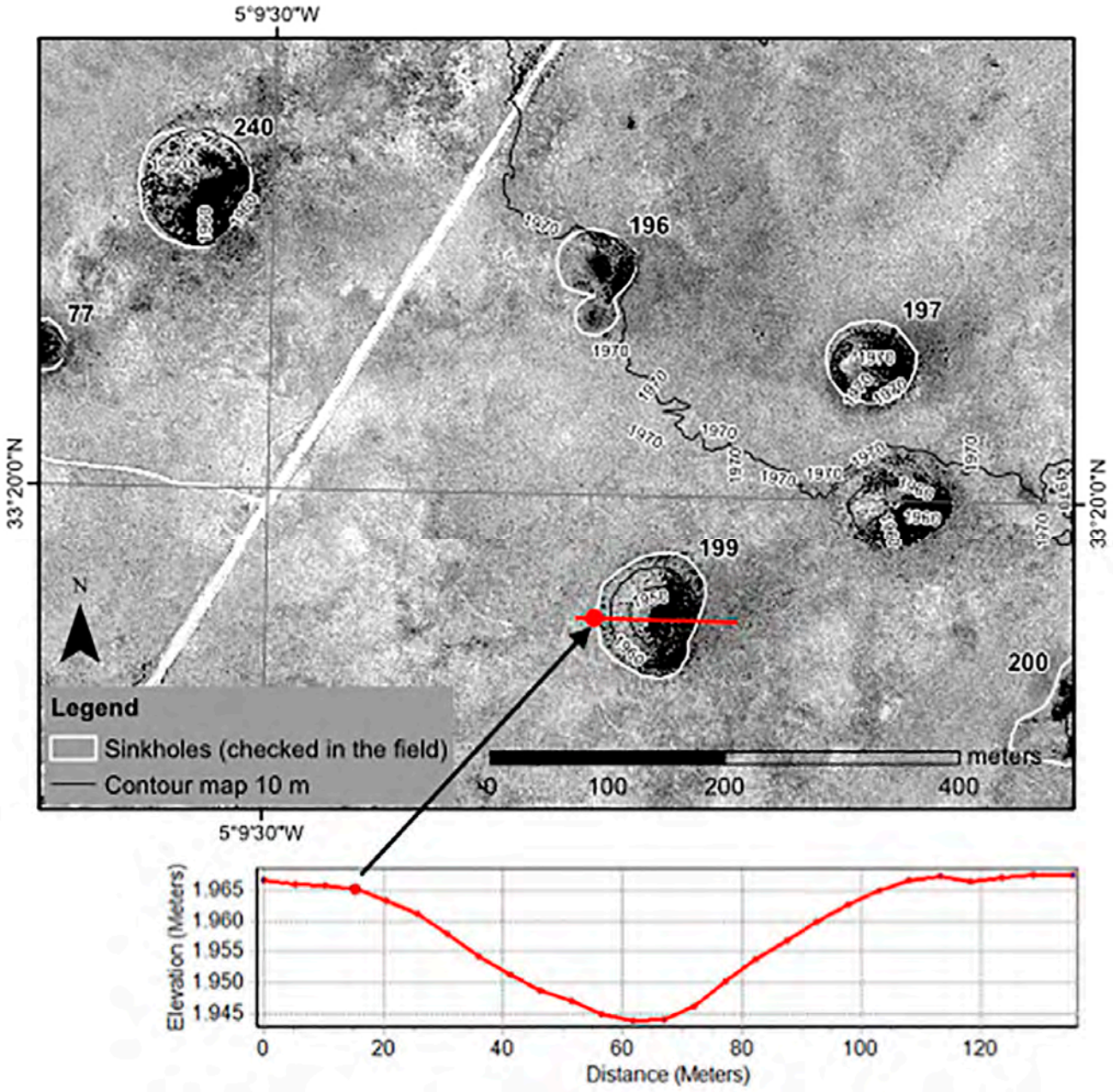

Figure 5. Orthoimage of a sector of the study area showing the good horizontal accuracy of the DEM extracted from Pleiades tri-stereo images. The elevation profiles, obtained from this DEM, demonstrate the correct position of the knickpoint along the border of the depressions, as mapped from photointerpretation. The contours confirm the results.

2.5. DEM Validation

In order to check the accuracy of the resulting DEM, and use it to extend the morphometric data collected in the field for a limited number of sinkholes with our elevation model, two separated methodologies were applied to extract the horizontal and vertical accuracies: (a) a qualitative evaluation of the horizontal accuracy was performed using the Pleiades orthoimages acquired in 2019, where the shapes of the sinkholes were overlaid (Figure 5); (b) the depth of the dolines was measured in the field using a Lietz Sokkisha (Now Sokkia, Tokyo) rangefinder with 50 cm base and an operating range of 10–250 m and an accuracy of around 5%. The data collected in the field were compared with the same parameters extracted from the DEM using statistical tests. The position of the dolines was acquired using a handheld rugged GPS (Trimble Juno equipped with the extension ESRI's ArcPad), allowing us to identify the previously numbered dolines (from Landsat

and ASTER images), and add the missing ones (not visible in the low-resolution satellite images). A total of 89 dolines were field checked.

The depth validation was performed making use of a non-parametric signed-rank Wilcoxon test for non-normal distributed samples using R software [30]. This test compared the field-based and the DEM-derived depth measurements to assess whether their distributions are significantly different. Additionally, Pearson's correlation test and linear regression models were calculated to compare the two datasets. The correlation coefficient is a statistical measure of the strength of the relationship between the relative movements of two variables. The correlation coefficient ranges between −1.0 (negative correlation) and +1.0 (positive correlation), with absolute values of 1 representing perfect correlations. These statistical tests were performed on the original field-based dataset (n = 89) and on a subset of the population after stripping of the outliers identified through R software (n = 84).

3. Results and Discussion

The morphometric parameters and the geometrical shape of the dolines (i.e., flat, funnel-shape, bowl-shape, mixed) were investigated in the GIS environment and compared with the measures collected in the field (Figures 6 and 7).

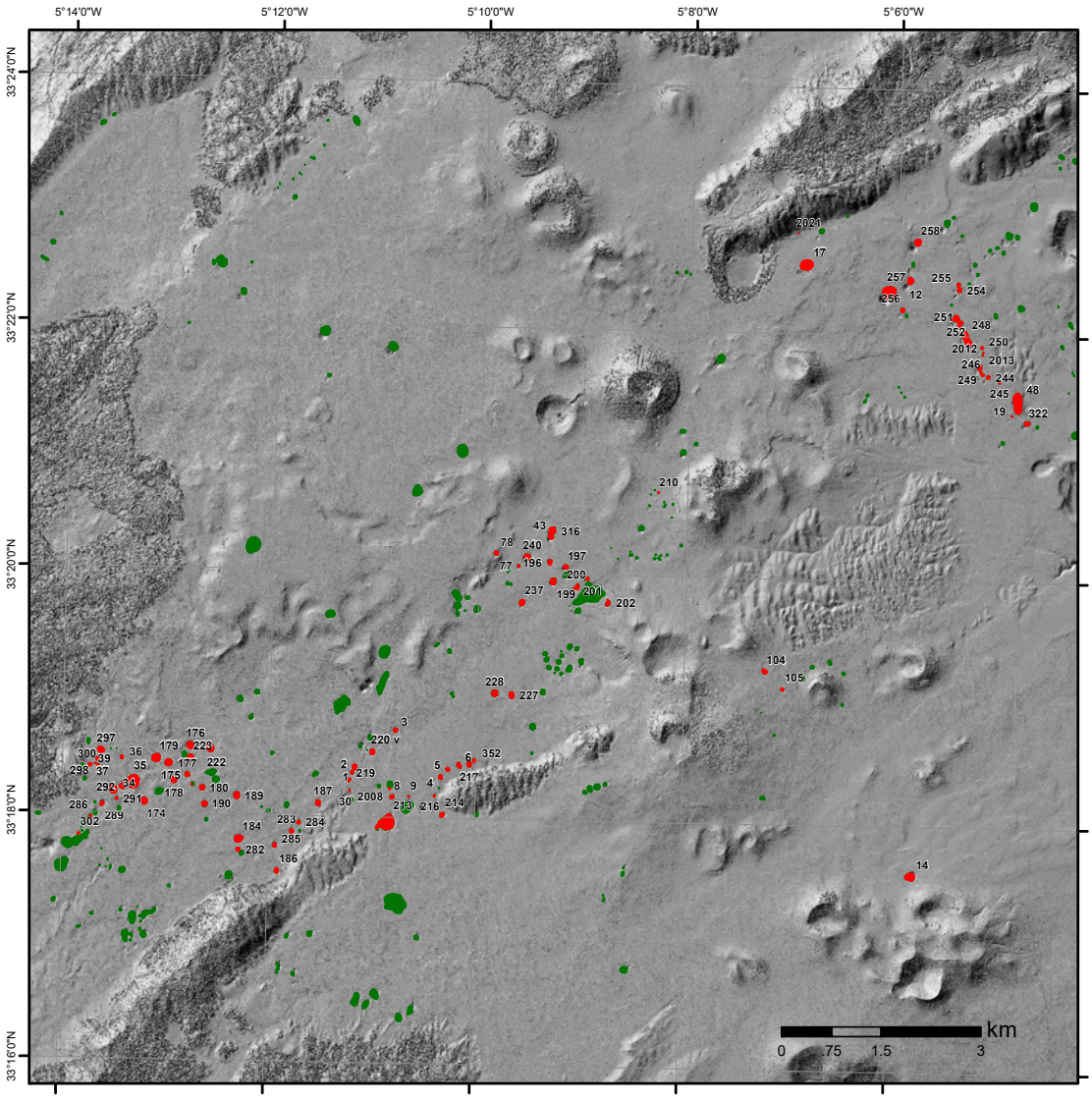

Figure 6. Shaded relief map extracted from the processing of the Pleiades-derived DEM of the study area. Sinkholes checked in the field and used to validate the DEM-derived morphometric parameters are reported in red; sinkholes identified from photointerpretation are shown in green.

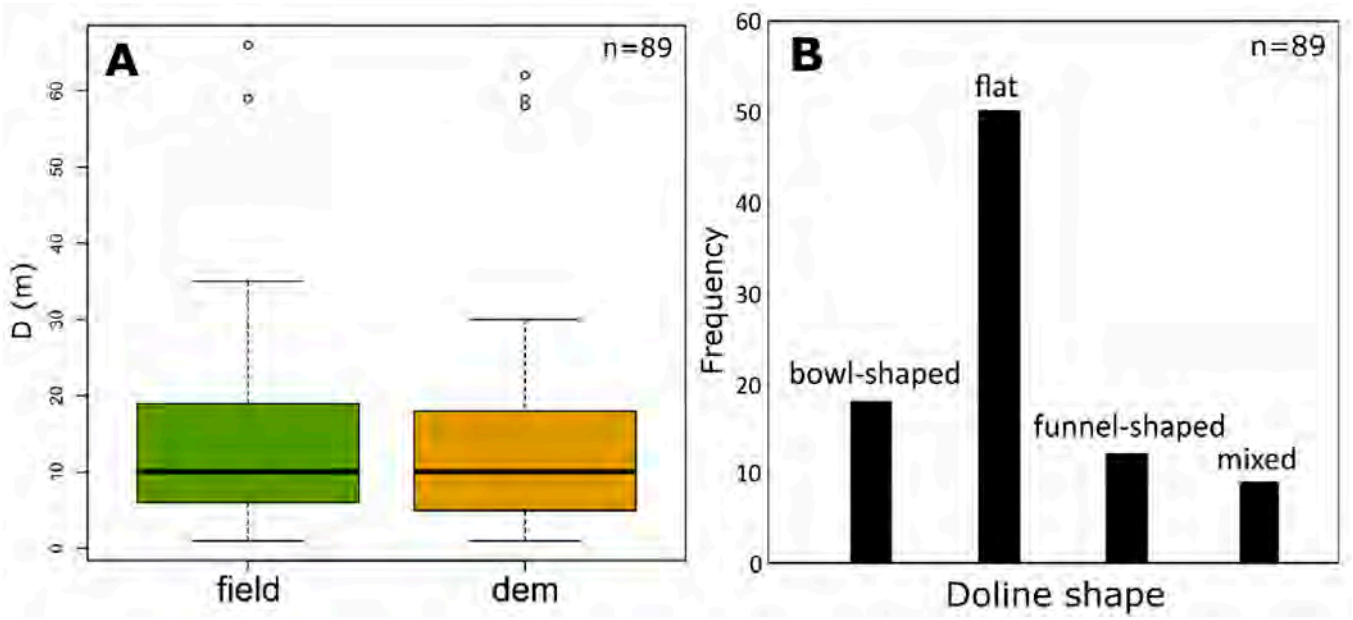

Figure 7. (**A**) Boxplots of the depth (D) of the dolines as calculated in the field (green boxplot) and using the DEM (orange boxplot). The limits of the boxes and whiskers represent respectively the first and third quartiles. The black lines inside the boxes represent the median values. (**B**) Frequency histogram of the doline shapes classified by type.

A total of 357 dolines were remotely recognized in this study. Of these, 89 were field-checked and validated (Table 3). Dolines range in shape from symmetric bowl-shaped depressions (n = 18), dolines with flat bottom (n = 50), funnel-shaped dolines (n = 12), and asymmetric dolines with mixed shapes (n = 9) (Figure 7).

Table 3. Summary table with the morphometric measurements of the 89 dolines investigated in this study.

TYPE	Doline ID	Depth_Field (m)	Z_Min (m)	Z_Max (m)	Z_Mean (m)	2D_Surf. (m^2)	Perimeter (m)	Depth_DEM (m)	ΔD (m)	|ΔD| (m)
bowl	251	17	1881	1892	1890	7733	264	11	−6	6
bowl	252	9	1883	1894	1890	12,457	350	11	2	2
bowl	1	28	1899	1920	1912	9203	263	21	−7	7
bowl	5	11	1916	1928	1924	5529	199	12	1	1
bowl	30	9	1912	1917	1915	2068	99	5	−4	4
bowl	34	10	1870	1883	1878	16,217	392	12	2	2
bowl	37	6	1883	1888	1887	4197	168	5	0	0
bowl	104	4	1961	1966	1964	7986	263	5	1	1
bowl	105	10	1948	1957	1953	3863	157	9	−2	2
bowl	174	26	1862	1892	1881	13,461	332	29	3	3
bowl	219	11	1910	1919	1915	3896	162	9	−2	2
bowl	237	27	1924	1948	1939	10,926	291	24	−4	4
bowl	283	7	1890	1896	1893	5338	200	7	0	0
bowl	297	3	1886	1889	1887	11,237	319	3	0	0
bowl	300	5	1884	1887	1886	2466	114	3	−2	2
bowl	316	17	1949	1970	1960	12,961	331	21	4	4
bowl	257	67	1851	1911	1890	48,579	662	60	−7	7
bowl	35	15	1871	1892	1884	35,182	601	21	6	6
flat	12	22	1883	1907	1898	13,071	330	24	2	2
flat	19	8	1863	1868	1866	1852	89	4	−3	3

Table 3. *Cont.*

TYPE	Doline ID	Depth_Field (m)	Z_Min (m)	Z_Max (m)	Z_Mean (m)	2D_Surf. (m^2)	Perimeter (m)	Depth_DEM (m)	ΔD (m)	|ΔD| (m)
flat	244	9	1874	1883	1880	4950	184	8	−1	1
flat	245	6	1877	1881	1879	2201	104	4	−1	1
flat	246	8	1878	1883	1882	2742	124	5	−3	3
flat	247	6	1879	1884	1882	2361	109	5	−2	2
flat	249	10	1871	1885	1881	8500	267	14	3	3
flat	250	6	1881	1886	1884	3518	147	5	0	0
flat	254	14	1891	1904	1900	6326	215	13	−1	1
flat	255	12	1895	1904	1902	4767	179	10	−2	2
flat	256	30	1888	1900	1895	6280	212	12	−18	18
flat	2012	4	1882	1885	1883	1589	79	3	−1	1
flat	2013	1	1883	1884	1884	989	49	1	0	0
flat	2021	2	1931	1934	1932	1234	152	3	1	1
flat	2	19	1905	1920	1914	4775	178	15	−5	5
flat	8	8	1912	1922	1917	6097	212	10	2	2
flat	9	1	1920	1922	1921	1999	98	2	1	1
flat	36	12	1882	1891	1888	4563	176	9	−3	3
flat	39	5	1881	1885	1884	4882	186	4	−1	1
flat	43	20	1946	1967	1959	9814	278	20	0	0
flat	77	6	1949	1954	1951	2896	128	5	−1	1
flat	78	6	1969	1977	1972	6351	221	8	2	2
flat	175	9	1889	1898	1893	7343	239	9	0	0
flat	176	6	1889	1901	1892	13,176	346	12	6	6
flat	177	10	1887	1901	1896	13,329	345	13	4	4
flat	178	18	1879	1898	1891	10,657	294	19	1	1
flat	186	6	1884	1892	1888	6969	235	8	2	2
flat	187	15	1891	1908	1902	8438	256	17	2	2
flat	189	13	1887	1901	1896	12,078	325	13	0	0
flat	190	15	1881	1897	1891	9044	267	16	1	1
flat	196	10	1951	1962	1958	7308	283	11	1	1
flat	197	26	1944	1966	1958	7655	236	22	−4	4
flat	210	2	1972	1973	1972	1790	89	2	0	0
flat	214	13	1910	1924	1918	7224	239	14	1	1
flat	216	4	1921	1924	1922	2156	102	4	0	0
flat	222	28	1873	1903	1893	15,912	368	29	1	1
flat	223	9	1886	1899	1893	9171	272	13	4	4
flat	240	22	1929	1956	1944	12,767	313	27	5	5
flat	282	5	1889	1893	1891	5631	205	4	−1	1
flat	284	6	1890	1898	1894	4590	177	7	2	2
flat	286	11	1871	1874	1872	3184	145	2	−9	9
flat	289	11	1866	1877	1871	5805	205	11	0	0
flat	291	8	1876	1883	1879	3261	138	7	−1	1
flat	292	4	1879	1884	1881	8703	270	5	1	1
flat	298	1	1885	1887	1886	1502	75	1	0	0
flat	302	3	1872	1875	1873	2640	122	3	0	0
flat	2008	3	1918	1921	1919	2206	104	3	0	0
flat	10	3	1898	1901	1899	1941	83	3	0	0
flat	48	13	1859	1874	1868	42,854	762	15	3	3
flat	14	30	1888	1919	1908	21,090	440	30	1	1
funnel	258	30	1882	1911	1899	13,515	330	29	−1	1
funnel	3	22	1911	1926	1920	6117	203	16	−7	7
funnel	4	20	1912	1927	1923	6821	219	15	−5	5
funnel	179	35	1880	1898	1891	18,253	401	18	−18	18
funnel	180	25	1879	1901	1894	9154	261	22	−2	2

Table 3. *Cont.*

TYPE	Doline ID	Depth_Field (m)	Z_Min (m)	Z_Max (m)	Z_Mean (m)	2D_Surf. (m^2)	Perimeter (m)	Depth_DEM (m)	ΔD (m)	|ΔD| (m)
funnel	201	17	1949	1963	1959	4608	172	14	−3	3
funnel	217	20	1910	1928	1922	7661	241	18	−2	2
funnel	227	26	1915	1940	1932	11,133	294	24	−2	2
funnel	228	32	1910	1939	1929	12,446	305	29	−3	3
funnel	220	25	1898	1919	1912	9029	261	21	−4	4
funnel	184	26	1868	1891	1885	16,469	386	23	−3	3
funnel	213	34	1860	1922	1900	61,677	869	62	28	28
mixed	322	11	1853	1864	1858	7505	249	11	0	0
mixed	6	15	1915	1929	1924	7672	254	13	−2	2
mixed	199	26	1934	1957	1949	12,229	317	24	−2	2
mixed	200	13	1948	1958	1955	8326	282	11	−2	2
mixed	202	10	1963	1972	1968	7782	265	9	−1	1
mixed	285	6	1885	1891	1888	5602	204	7	1	1
mixed	352	9	1921	1928	1925	5237	194	7	−2	2
mixed	17	60	1882	1940	1917	50,258	569	58	−1	1
mixed	248	8	1873	1891	1886	26,056	591	18	10	10

Extracted depressions range in depth from a minimum of 1 to a maximum of 62 m. Doline perimeters vary between 49 and 868 m, whereas their plan surfaces range between 989 and 61,677 m^2.

To evaluate the accuracy of the extracted depth values, statistical tests were performed as described in Section 2.5. The results (*p*-values) of the tests are reported in Table 4. The signed-rank Wilcoxon tests indicate no significant variations between the two paired distributions (*p*-value > 0.05) both for the entire population and the subset without outliers.

Table 4. Results of the statistical tests of the population with and without outliers.

Dataset	Shapiro-Wilk Normality Test	Wilcoxon Signed-Rank Test		Pearson's Correlation Test
		p-Value		*Correlation Coefficient*
D_field	8.49×10^{-6}	0.063	2.20×10^{-16}	0.91
D_dem	7.90×10^{-7}			
D_field without outliers	3.53×10^{-6}	0.064	2.20×10^{-16}	0.97
D_dem without outliers	1.06×10^{-5}			

The differences between the depth measured in the field and those extracted from the DEM (ΔD) for each doline are shown in the boxplots of Figure 7, classified by type. The summary of the basic statistics calculated for the datasets is reported in Table 5. The difference ΔD represents a measure of the vertical accuracy of the DEM extracted from Pleiades tri-stereo images.

Table 5. Basic statistics of the depth (D) and depth difference (ΔD) of the investigated dolines.

	D_Field (m)	D_Dem (m)	ΔD (m)—All Measures	ΔD (m)—No Outliers
minimum	1	1	0	0
first quartile	6	5	1	1
median	11	11	2	2
mean	14	14	3	2
third quartile	20	18	3	3
maximum	67	62	28	7
st. deviation	11	12	4	2

The boxplots in Figure 8 testify a good accuracy of the population without outliers (mean ΔD value of 2 ± 2 m). The dataset with outliers shows a mean ΔD value of 3 ± 4 m. The main differences represented by the 5 dolines identified as outliers range from 9 to 28 m, whereas the maximum error in the dataset without outliers is 7 m. As shown in the right boxplots of Figure 8, the main errors (both mean and median >2 m) are referred to funnel-shaped and bowl-shaped dolines.

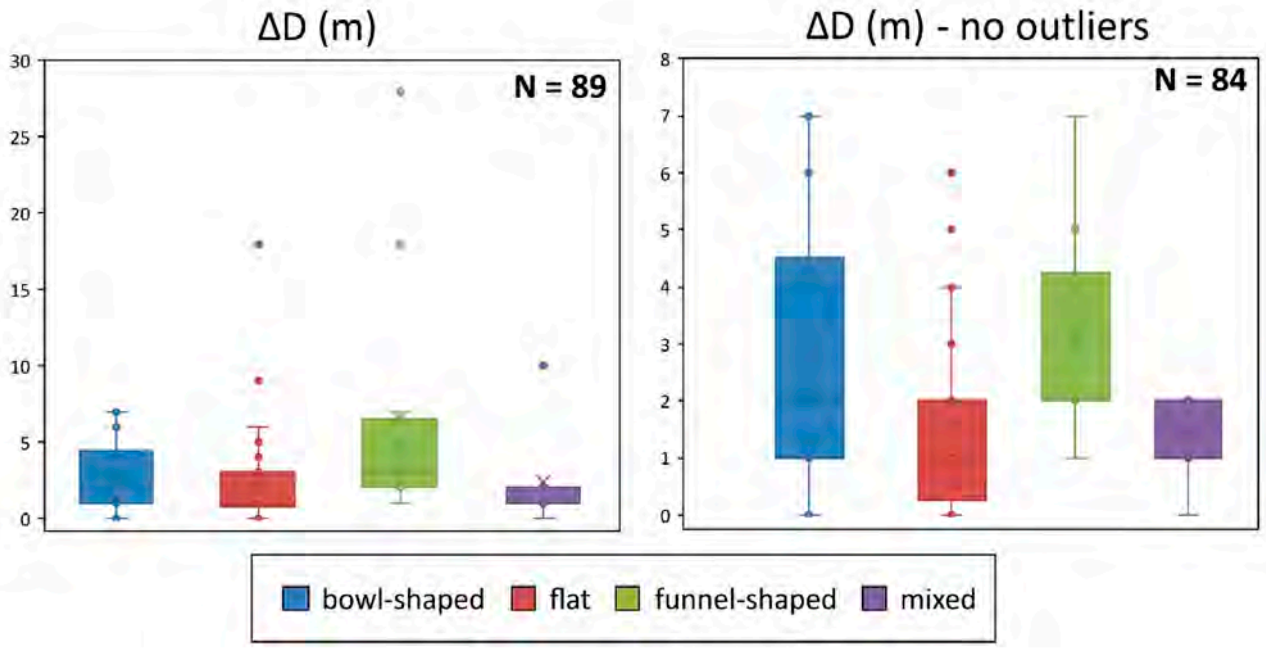

Figure 8. Boxplots of the difference between depth (D) values from field- and DEM-derived measurements for the entire population (**left**) and a subset without outliers (**right**). The boxplots are grouped according to doline shape. The limits of the boxes and whiskers represent the first and third quartiles, respectively. The straight lines inside the boxes represent the median values and the crosses represent the mean values.

Other measures of the accuracy of the depth extracted from the DEM are shown in the scatterplots of Figure 8 and in the results of the Pearson's correlation tests in Table 4. The resulting *p*-value (<<0.05) and correlation coefficients (>0.9) indicate a good positive correlation between the values derived from field and DEM measurements, with an excellent correlation coefficient of 0.97 for the dataset without outliers.

Furthermore, the linear regression best-fit models calculated for the entire population (Figure 9A) and the subset without outliers (Figure 9B) show high R^2 values of 0.83 and 0.95, respectively. The slope of the trend lines (a value of 1 would mean a perfect match between field and DEM derived measurements) is 0.91 confirming a good accuracy of our DEM. The dolines with the highest errors are those presenting dense vegetation cover or human-built structures that obscure the view of the real bottom surface (Figure 10).

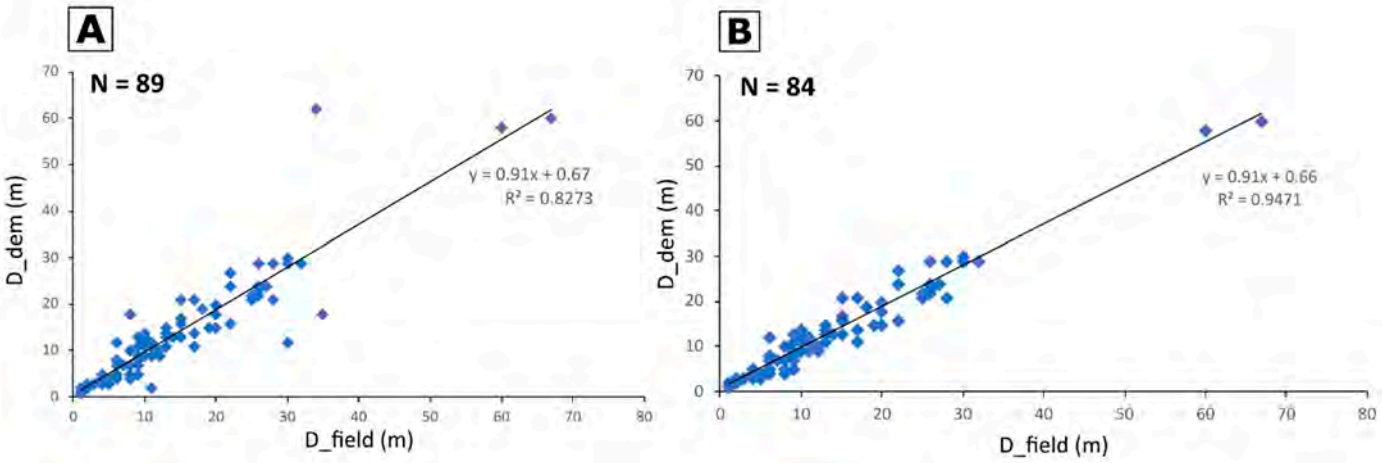

Figure 9. (**A**) Scatterplot of the depth (D) measures calculated in the field and in the DEM for the entire population (N = 89). (**B**) Scatterplot of the subset without outliers (N = 84). Lines represent the best-fit of the linear regression model.

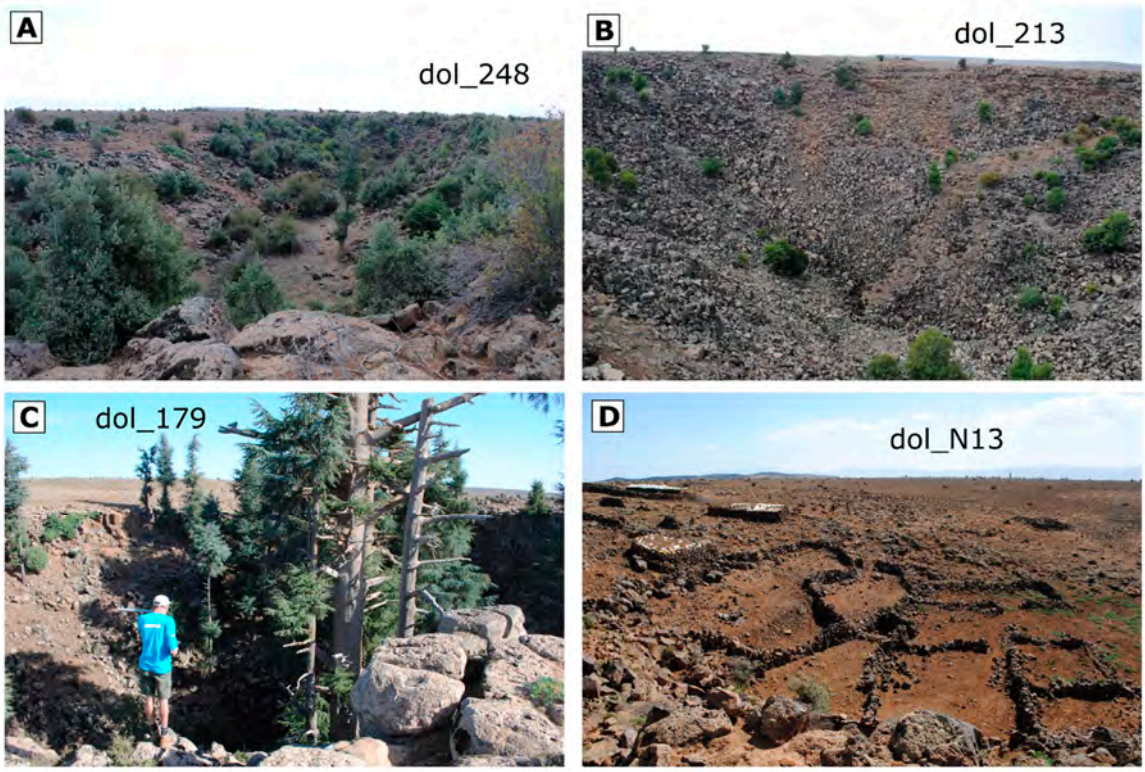

Figure 10. Examples of typical dolines that produced the highest depth differences. (**A**) mixed geometry doline with dense vegetation and boulders; (**B**) funnel-shaped deep doline with blocks and boulders on the bottom; (**C**) funnel-shaped doline with high trees covering the bottom; (**D**) shallow flat-shaped doline with dry stone walls at the bottom and near the knickpoints.

4. Conclusions

The use of high-resolution satellite imagery and digital elevation models (DEM) for the extraction of morphometric parameters of different positive and negative landforms is extremely useful especially over large and remote areas where detailed topographic maps are not available. The Pleiades satellite constellation delivers images with a ground resolution of 0.5 m, and their use in a GIS environment allows to automatically extract very precise planimetric measurements. We used Pleiades images to extract morphometric measurements of the doline fields opening in the basaltic plateau of Azrou, in the Middle Atlas (Morocco). To verify the accuracy of the vertical measurements calculated from the

Pleiades-derived DEM, we carried out a ground-truthing on a subset of 89 different dolines (out of a total of 357 identified using low-resolution satellite data including LANDSAT 7 ETM+, ASTER, and ESA Sentinel 2). We found an overall good correlation (p-value < 0.05 and correlation coefficient >0.9) between the DEM-derived depths and those measured with telemeter in the field. The largest differences were obtained on deep funnel-shaped dolines and on shallow bowl-shaped dolines, where disturbance is created by tall trees, human-built structures (dry walls), boulders, or a combination of these features.

Our study shows that very-high-resolution satellite images such as Pleiades (0.5 m ground resolution), are extremely useful in obtaining precise planimetric measurements on large landforms such as dolines. DEMs extracted from Pleiades stereo images deliver good results on the vertical scale if doline floors are not masked by vegetation or disturbed by large debris (boulders or dry walls), with mean depth errors of 2 ± 2 m.

These results will allow for extending the information extracted in the field to the dolines present in inaccessible areas of the plateau, allowing to obtain more information to complete their morphological profiling and propose a model on their unknown origin.

The results of our work demonstrate that tri-stereo satellite images are suitable for the morphometric assessment of shadow-prone negative and positive landforms, and might also be used for the analysis of skylights and collapses on lava flows on the Moon and on Mars, where vegetation or human-built structures are completely lacking, as preparatory surveys for future robotic and human explorations of extraterrestrial caves [31–33].

Author Contributions: M.T.M., L.P. and J.D.W. wrote the original draft and performed the editing of the manuscript. M.T.M. performed the DEM extraction and the morphometric measurements; M.T.M. and J.D.W. performed the fieldwork in 2016; L.P. performed the statistical analyses and DEM validation. All authors have read and agreed to the published version of the manuscript.

Funding: Pleiades images were granted in 2018 in the framework of the project entitled "The Azrou Plateau (Middle Atlas, Morocco): a perfect terrestrial analogue for studying both karst and lava tube collapses with remote sensing techniques" (RITM0042620—ESA-TPM4 Project Proposal id43487, PI MTM). Fieldwork was carried out in Autumn 2016 in the project "The Azrou Plateau (Middle Atlas, Morocco): a perfect terrestrial analogue for studying both karst and lava tube collapses with remote sensing techniques and field geology, Europlanet project 16-EPN2-007 (PI JDW).

Institutional Review Board Statement: Not applicable.

Informed Consent Statement: Not applicable.

Data Availability Statement: All supporting data are included in this paper.

Acknowledgments: This study has been carried out in the framework of the project "The Azrou Plateau (Middle Atlas, Morocco: a perfect terrestrial analogue for studying both karst and lava tube collapses with remote sensing techniques", approved by ESA, that allows access to Spot and Pleiades as ESA's Third-Party Mission. Thanks also to Europlanet who provided funding for fieldwork in 2016 (Europlanet project 16-EPN2-007, PI JDW). Pictures of Figure 10 are courtesy of Sergio Passanante.

Conflicts of Interest: The authors declare no conflict of interest. The funders had no role in the design of the study; in the collection, analyses, or interpretation of data; in the writing of the manuscript, or in the decision to publish the results.

References

1. Melis, M.T.; Mundula, F.; Dessì, F.; Cioni, R.; Funedda, A. Tracing the Boundaries of Cenozoic Volcanic Edifices from Sardinia (Italy): A Geomorphometric Contribution. *Earth Surf. Dyn.* **2014**, *2*, 481–492. [CrossRef]
2. Florinsky, I.V. An Illustrated Introduction to General Geomorphometry. *Prog. Phys. Geogr. Earth Environ.* **2017**, *41*, 723–752. [CrossRef]
3. Vörös, F.; van Wyk de Vries, B.; Karátson, D.; Székely, B. DTM-Based Morphometric Analysis of Scoria Cones of the Chaîne Des Puys (France)—The Classic and a New Approach. *Remote Sens.* **2021**, *13*, 1983. [CrossRef]

4. De Carvalho, O.A.; Guimarães, R.F.; Montgomery, D.R.; Gillespie, A.R.; Trancoso Gomes, R.A.; De Souza Martins, É.; Silva, N.C. Karst Depression Detection Using ASTER, ALOS/PRISM and SRTM-Derived Digital Elevation Models in the Bambuí Group, Brazil. *Remote Sens.* **2014**, *6*, 330–351. [CrossRef]
5. Mihevc, A.; Mihevc, R. Morphological characteristics and distribution of dolines in Slovenia, a study of a lidar-based doline map of Slovenia. *Acta Carsologica* **2021**, *50*, 11–36. [CrossRef]
6. Öztürk, M.Z.; Şimşek, M.; Şener, M.F.; Utlu, M. GIS based analysis of doline density on Taurus Mountains, Turkey. *Environ. Earth Sci.* **2018**, *77*, 1–13. [CrossRef]
7. Telbisz, T. Lidar-Based Morphometry of Conical Hills in Temperate Karst Areas in Slovenia. *Remote Sens.* **2021**, *13*, 2668. [CrossRef]
8. Theilen-Willige, B.; Malek, H.A.; Charif, A.; El Bchari, F.; Chaïbi, M. Remote Sensing and GIS Contribution to the Investigation of Karst Landscapes in NW-Morocco. *Geosciences* **2014**, *4*, 50–72. [CrossRef]
9. Moreno-Gómez, M.; Liedl, R.; Stefan, C. A New GIS-Based Model for Karst Dolines Mapping Using LiDAR.; Application of a Multidepth Threshold Approach in the Yucatan Karst, Mexico. *Remote Sens.* **2019**, *11*, 1147. [CrossRef]
10. Pisani, L.; De Waele, J. Candidate Cave Entrances in a Planetary Analogue Evaporite Karst (Cordillera de La Sal, Chile): A Remote Sensing Approach and Ground-Truth Reconnaissance. *Geomorphology* **2021**, *389*, 107851. [CrossRef]
11. Chen, H.; Oguchi, T.; Wu, P. Morphometric Analysis of Sinkholes Using a Semi-Automatic Approach in Zhijin County, China. *Arab. J. Geosci.* **2018**, *11*, 412. [CrossRef]
12. Bauer, C. Analysis of Dolines Using Multiple Methods Applied to Airborne Laser Scanning Data. *Geomorphology* **2015**, *250*, 78–88. [CrossRef]
13. Rieg, L.; Klug, C.; Nicholson, L.; Sailer, R. Pléiades Tri-Stereo Data for Glacier Investigations—Examples from the European Alps and the Khumbu Himal. *Remote. Sens.* **2018**, *10*, 1563. [CrossRef]
14. Deilami, K.; Hashim, M. Very High Resolution Optical Satellites for DEM Generation: A Review. *EJSR* **2011**, *49*, 542–554.
15. Sefercik, U.G.; Alkan, M.; Buyuksalih, G.; Jacobsen, K. Generation and Validation of High-Resolution DEMs from Worldview-2 Stereo Data. *Photogramm. Rec.* **2013**, *28*, 362–374. [CrossRef]
16. Bhushan, S.; Shean, D.; Alexandrov, O.; Henderson, S. Automated Digital Elevation Model (DEM) Generation from Very-High-Resolution Planet SkySat Triplet Stereo and Video Imagery. *ISPRS J. Photogramm. Remote. Sens.* **2021**, *173*, 151–165. [CrossRef]
17. Bagnardi, M.; González, P.J.; Hooper, A. High-Resolution Digital Elevation Model from Tri-Stereo Pleiades-1 Satellite Imagery for Lava Flow Volume Estimates at Fogo Volcano. *Geophys. Res. Lett.* **2016**, *43*, 6267–6275. [CrossRef]
18. Gleyzes, M.A.; Perret, L.; Kubik, P. Pleiades System Architecture and Main Performance. *Int. Arch. Photogramm. Remote. Sens. Spat. Inf. Sci.* **2012**, *39*, 537–542. [CrossRef]
19. Panagiotakis, E.; Chrysoulakis, N.; Charalampopoulou, V.; Poursanidis, D. Validation of Pleiades Tri-Stereo DSM in Urban Areas. *ISPRS Int. J. Geo-Inf.* **2018**, *7*, 118. [CrossRef]
20. Antonić, O.; Hatic, D.; Pernar, R. DEM-Based Depth in Sink as an Environmental Estimator. *Ecol. Model.* **2001**, *138*, 247–254. [CrossRef]
21. De Waele, J.; Melis, M.T. Geomorphology and Geomorphological Heritage of the Ifrane-Azrou Region (Middle Atlas, Morocco). *Environ. Geol.* **2009**, *58*, 587–599. [CrossRef]
22. Harmand, C.; Cantagrel, J.M. Le Volcanisme Alcalin Tertiaire et Quaternaire Du Moyen Atlas (Maroc): Chronologie K/Ar et Cadre Géodynamique. *J. Afr. Earth Sci.* **1984**, *2*, 51–55. [CrossRef]
23. Martin, J. Le Moyen Atlas central. Etude géomorphologique. *Notes Mémoires Serv. Géologique Maroc* **1981**, *258*, 1–446.
24. Williams, P. Dolines. In *Encyclopedia of Caves and Karst Science*; Gunn, J., Ed.; Fitzroy Dearborn: New York, NY, USA, 2004; pp. 628–642.
25. Menjour, F.; Remmal, T.; Hakdaoui, M.; El Kamel, F.; Lakroud, K.; Amraoui, F.; El-Amrani ERl Hassani, I.-E.; Van Wyk de Vries, B.; Boivin, P. Role of Fracturing in the Organization of the Karst Features of Azrou Plateau (Middle Atlas, Morroco) Studied by Remote Sensing Imagery. *J. Indian Soc. Remote Sens.* **2017**, *45*, 1015–1030. [CrossRef]
26. Muzirafuti, A.; Boualoul, M.; Barreca, G.; Allaoui, A.; Bouikbane, H.; Lanza, S.; Crupi, A.; Randazzo, G. Fusion of Remote Sensing and Applied Geophysics for Sinkholes Identification in Tabular Middle Atlas of Morocco (the Causse of El Hajeb): Impact on the Protection of Water Resource. *Resources* **2020**, *9*, 51. [CrossRef]
27. Barakat, A.; El Baghdadi, M.; Rais, J.; Aghezzaf, B.; Slassi, M. Assessment of spatial and seasonal water quality variation of Oum Er Rbia River (Morocco) using multivariate statistical techniques. *Int. Soil Water Conserv. Res.* **2016**, *4*, 284–292. [CrossRef]
28. Poli, D.; Remondino, F.; Angiuli, E.; Agugiaro, G. Radiometric and Geometric Evaluation of GeoEye-1, WorldView-2 and Pléiades-1A Stereo Images for 3D Information Extraction. *ISPRS J. Photogramm. Remote Sens.* **2015**, *100*, 35–47. [CrossRef]
29. Vacca, A.; Loddo, S.; Melis, M.T.; Funedda, A.; Puddu, R.; Verona, M.; Fanni, S.; Fantola, F.; Madrau, S.; Marrone, V.A.; et al. A GIS Based Method for Soil Mapping in Sardinia, Italy: A Geomatic Approach. *J. Environ. Manag.* **2014**, *138*, 87–96. [CrossRef] [PubMed]
30. David, F. Constructing confidence sets using rank statistics. *J. Am. Stat. Assoc.* **1972**, *67*, 687–690.
31. Titus, T.N.; Wynne, J.J.; Malaska, M.J.; Agha-Mohammadi, A.; Buhler, P.B.; Alexander, E.C.; Ashley, J.W.; Azua-Bustos, A.; Boston, P.J.; Buczkowski, D.L.; et al. A Roadmap for Planetary Caves Science and Exploration. *Nat. Astron.* **2021**, *5*, 524–525. [CrossRef]

32. Titus, T.; Wynne, J.J.; Boston, P.; de Leon, P.; Demirel-Floyd, C.; Jones, H.; Sauro, F.; Uckert, K.; Aghamohammadi, A.; Alexander, C.; et al. Science and Technology Requirements to Explore Caves in Our Solar System. *Bull. AAS* **2021**, *53*, 167. [CrossRef]
33. Scaioni, M.; Giommi, P.; Brunetti, M.T.; Carli, C.; Cerroni, P.; Cremonese, G.; Forlani, G.; Gamba, P.; Lavagna, M.; Melis, M.T.; et al. The "Moon Mapping" Project to Promote Cooperation between Students of Italy and China. *ISPRS Int. Arch. Photogramm. Remote Sens. Spat. Inf. Sci.* **2016**, *41*, 71–78. [CrossRef]